



SARAO

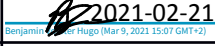


South African Radio
Astronomy Observatory

Organisation : NRF (National Research Foundation)
Facility : SARAO (South African Radio Astronomy Observatory)
Project : MeerKAT
Document Type : Commissioning report

Modelling of PKS B 1934-638 (J193925.0-634245) as UHF and L-Band calibrator for MeerKAT

Document Number	M2600-0000-043
Revision	B
Classification	Public
Prepared by	Benjamin Hugo
Date	2021-02-21

DOCUMENT APPROVAL

	Name	Designation	Affiliation	Signature/Date
Prepared by	Benjamin Hugo	Junior Software Developer, RARG	SARAO	 Benjamin Hugo (Mar 9, 2021 15:07 GMT+2)
Reviewed by	Emil Lenc	Senior scientist	CSIRO	
	Tom Mauch	Senior scientist	SARAO	 Thomas Mauch (Mar 11, 2021 09:57 GMT+2)
Approved by	Sharmila Goedhart	Division head: commissioning	SARAO	 Sharmila Goedhart (Mar 11, 2021 10:18 GMT+2)

DOCUMENT HISTORY

Revision	Date of Issue	Prepared by	Comments (e.g. ECN Number or changes to document)
A	2020-04-18	Benjamin Hugo	Draft for review
B	2021-02-21	Benjamin Hugo	Revision comments taken into consideration - discussion of residuals. Improved SEFD measurement and more detailed discussion. Notes on L-band HDR limitations in CASA.

DOCUMENT SOFTWARE

	Package	Version	Filename
Word Processor	Google Drive		N/A
Block Diagrams			N/A
Other	CASA	4.7.2	N/A
	WSClean	2.5	
	Cubical	#34485fd3a8c3e7a5d	

ORGANISATION DETAILS

Name	SARAO, Cape Town Office (Observatory, Western Cape)	SARAO, Johannesburg Office (Rosebank, Gauteng)
Registered Address	2 Fir Street, Black River Park (North), Observatory, Cape Town, 7925, South Africa	1st Floor, 17 Baker Street Rosebank, Gauteng 2196, South Africa
Telephone	+27 (0) 21 506 7300	+27 (0) 11 268 3400
Fax.	+27 (0) 21 506 7375	+27 (0) 11 442 2454
Website	www.sarao.ac.za	www.sarao.ac.za

TABLE OF CONTENTS

Motivation	5
Problem illustration from observations of PKS B1934-638 at UHF band	6
Observation and data calibration	9
Long term stability analysis	11
Field modelling of PKS B1934-638	12
UHF: Derivation of full sky model	12
UHF: System Equivalent Flux Density estimation	13
UHF: Application requirements for Science Processor UHF transfer calibration	15
Derivation of a companion L-Band full sky model and comparison to ASKAP	17
HDR imaging at L-Band	18
References	19
Appendix A	19

GLOSSARY

Crosshand: The $X_p Y_q^*$ and $Y_p X_q^*$ correlations.

Parallelhand: The $X_p X_q^*$ and $Y_p Y_q^*$ correlations.

X Feed: Horizontal (H) feed according to convention defined by KATdal

Y Feed: Vertical (V) feed according to convention defined by KATdal

GPS: Gigahertz Peaked Source

FWHM: Full width half maximum of the antenna far-field voltage response.

SEFD: System Equivalent Flux Density

1 Motivation

This document details the calibration procedure used to model UHF and L-Band flux calibrators for the 2018 layout of the MeerKAT telescope, that is the core-dominated 7.69km layout with L and UHF band receivers. We derive spatio-spectral models necessary for calibration of a sensitive wideband widefield receiver system.

The combination of widefield sensitivity and large instrumental bandwidth poses a problem for first order calibration of SKA-MID and its precursors. The desired line-to-line spectral dynamic range in excess of -30dB requires careful calibration of the system frequency (hereafter “bandpass”) response.

The traditional modelling approach as implemented in standard calibration routines (e.g. NRAO CASA) is applicable only to narrowband, narrowfield instruments, where the instrument has limited instantaneous sensitivity to off-axis sources. This traditional calibration method is no longer effective for spectral studies in the precursor era, where the off axis source contribution to the sampled spatial frequencies is on levels comparable and exceeding the continuum subtraction specification of the system.

The problem can best be illustrated at hand of the definition of the 2 source visibility function of a two element interferometer. Consider a point source calibrator at the phase centre with a flux density S_0 , and a second source of (beam modulated) flux density S_1 within the antenna primary beam at cosine coordinate $(x_1, 0)$. The analytic expression for the Fourier transform of these two unresolved sources yields the visibility function,

$$V(u(t, \nu), v(t, \nu)) = S_0 + S_1 e^{-i\phi}, \text{ where } \phi = 2\pi u(t, \nu) x_1$$

From Euler’s formula, the measured intensity is:

$$|V(u(t, \nu), v(t, \nu))| = \sqrt{S_0^2 + S_1^2 + 2S_0 S_1 \cos(-\phi)}$$

Similarly the measured phase is then:

$$\arg(V(u(t, \nu), v(t, \nu))) = \tan^{-1} \left(\frac{S_1 \sin(-\phi)}{S_0 + S_1 \cos(-\phi)} \right)$$

The intensity and phase are both periodic functions with time and frequency dependence that are coupled to the projected baseline length, as well as the distance of the secondary source from the phase centre. For $S_0 \gg S_1$ the phase term tends to 0, whereas for $S_0 \rightarrow S_1$

$$\arg(V(u(t, \nu), v(t, \nu))) = \tan^{-1} \left(\frac{\sin(-\phi)}{2 \cos^2(-\phi/2)} \right)$$

The phase term dependence becomes purely hour-angle dominated.

The equations here can be generalized to arbitrary numbers of off-axis sources: each source within the antenna or station primary beam and even strong sources in the beam sidelobes contributes such “ripples” to the visibility function in this manner.

Instrument calibration entails minimization of the negative log-likelihood between the measured visibilities and a per antenna complex gain-weighted model, along the following electronic description of the system response to a voltage product:

$$\epsilon = (D(t, \nu) - G_p(t, \nu)E_p(t, \nu)E_q^H(t, \nu)G_q^H(t, \nu))^H \sum^{-1} (D(t, \nu) - G_p(t, \nu)E_p(t, \nu)E_q^H(t, \nu)G_q^H(t, \nu))$$

E_p and E_q are complex voltages for each of the orthogonal receiver hands for a two station interferometer at a instantaneous spatial projection, D is the corresponding measured visibility data and Σ^{-1} is the weighted covariance. G_p and G_q are complex 2x2 Jones matrices for an interferometer between stations p and q .

It is easy to conceptually see how neglecting the off axis sources will result in absorption of the flux and phases into the complex antenna voltage gains. Depending on the solution interval size and cuts based on baseline length, the off-axis cosine components of the complex norm and arguments tend to diminish over time due to the rotating fringes of the interferometer.

Indeed one may argue that the effect is minimized by either careful selection of solution intervals. We show that for short calibrator scans the second order terms in the norm are prominent for a calibrator field with compact emission in close vicinity to the calibrator source, and the ripples do not wash away. The induced ripple structure can clearly be seen on derived gain solutions at levels comparable to the contributing off axis sources.

If transferred to a target field such solutions will imprint spectro-temporal errors on compact and diffuse structure alike, limiting achievable subtraction dynamic range to the modelling error introduced during transfer calibration. Depending on choice of imaging weights the spectral scale of the spectro-temporal ripples can mimic the scales expected from velocity ranges of HI emission. The reader is referred to detailed observational simulations presented by Heywood et al (2020).

It is also worth pointing out that the first order terms in this quadrature product are not hour angle dependent, and are therefore not washed out by the time-variable fringes of the interferometer. Neglect to include the off-axis sources will, in turn, also bias the average flux level of the system (and therefore the flux scales of continuum surveys).

We find off-axis structure an order of magnitude above the desired -30dB line-to-line subtraction dynamic range level at L-Band and two orders of magnitude above in the case of UHF on the most commonly-used flux calibrators. To limit the potential science impact we derive full spatial models, which are to be incorporated into the MeerKAT Science Data Processor for routine system phase and flux calibration.

2 Problem illustration from observations of PKS B1934-638 at UHF band

PKS B1934-638 is a standard flux calibrator for MeerKAT and other observatories such as the AT Compact Array. It is a Gigahertz-Peaked (GPS) quasar that is known to be temporally stable (Reynolds, 1994), Figure 1. It has also been shown in previous work to be unpolarized at levels well below -30 dB.

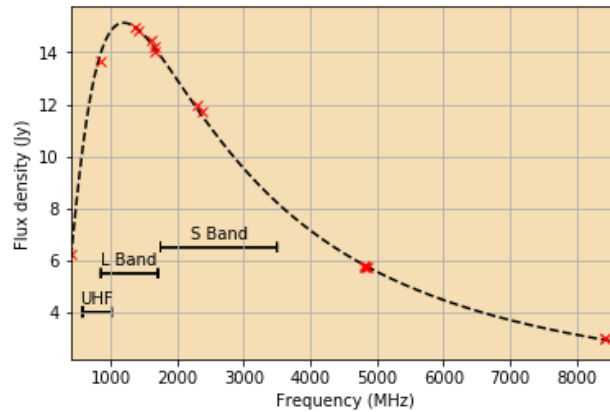


Figure 1: PKS B1934-638 Gigahertz peaked spectrum (Reinolds '94)

The source spectrum has strong curvature and turns over within the MeerKAT L-band. The inverted spectrum of the source at MeerKAT UHF band makes the source less than ideal for bandpass calibration at those frequencies. This coupled with a wider antenna primary beam (ie. increased widefield sensitivity) means the surrounding mJy AGN population contribute a significant fraction of the total flux induced on the system. We find fractional off-axis contributions at levels between $\sim 40\%$ and 20% for the first half of the bandwidth, of which the first ~ 100 MHz is substantially affected. We construct a model of the AGN population and simulate the visibilities corresponding to the field down to 10s of mJy without noise to illustrate the effect projection-dependent ripples on visibility phases for various baseline lengths (blue to red scale corresponding to the range $[-180, +180]$). The x-axis is coarsely channelized to the full 544 MHz fractional bandwidth. See Figure 2. Similarly the time-variant amplitude shows similar spectro-temporally variable ripples. Visibility amplitudes for various spacings are plotted for multiple times in Figure 3. We in turn verified that the ripples in frequency and in time illustrated here correspond to a high degree to the ripple structure seen from real observation using a selection of baselines - both in norm scale and length scales.

The (noiseless) simulated data was then calibrated against the Reynolds (1994) model without the structure included as per the standard point source calibration assumption of the CASA setjy and bandpass combination regularly employed in calibration pipelines. We varied the solution interval and the baseline length cuts imposed, as indicated in the legend in the figures to the right and found that only the large-scale ripple structure washed out to any extent, with the high frequency ripples remaining at similar scales. We plot the channel-normalized bandpass solution to emphasize the induced ripple error.

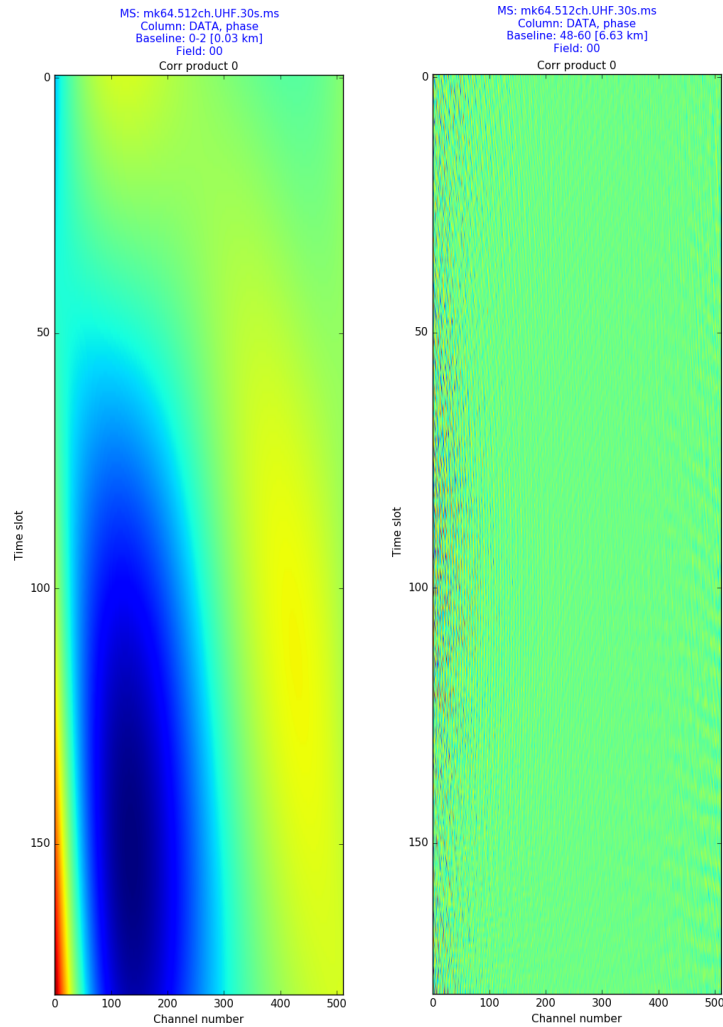


Figure 2: Effects of off axis sources on visibility phases on 0.03 km (left) and 6.63 km (right) baselines. Due to the GPS turnover of B1934-638 substantial phase variations are noticed on the lower frequencies of the band. The effects are most pronounced on short spacings indicating that the phase is contributed by resolved sources.

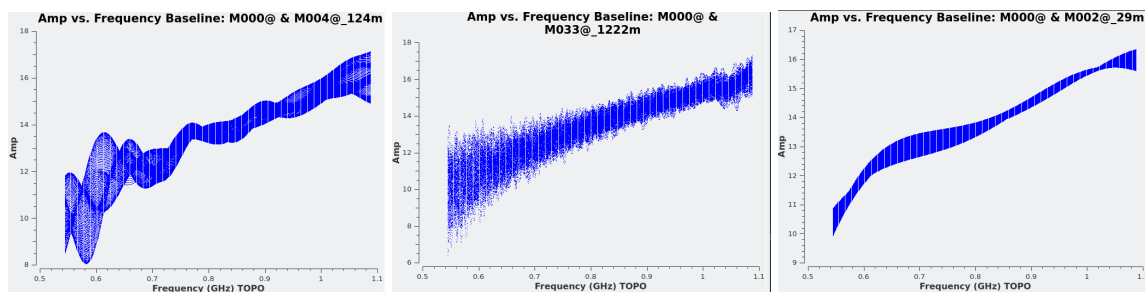
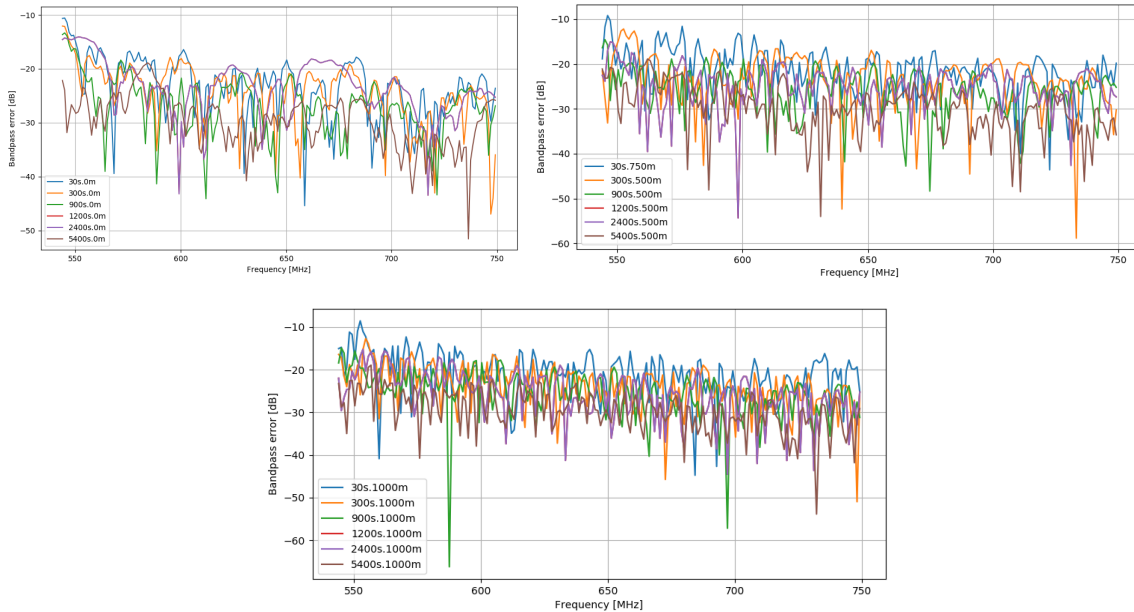


Figure 3: Effects of off-axis sources on visibility amplitudes as a function of baseline length from 0.124, 1.22, 0.029 km left to right respectively. Multiple time slots are overplotted to illustrate the time-variability of the visibility ripples

Figure 4: Amplitude gain absorbed ripples as a function of frequency for various baseline length cuts and solution intervals, for an arbitrarily chosen antenna. Neither longer solution intervals, nor stringer uv cutoffs have any noticeable effects on the peak error, aside from changing the length scales of the absorbed ripples.



3 Observation and data calibration

A dedicated UHF track was received for modelling of PKSB 1934-638 and PKSB 0407-65 22 Sep 2019. We additionally crawled the archive for L-band data where the two mentioned calibrators were observed with the standard VLA crosshand calibrator 3C286 for a long term study of the stability and polarimetric properties of the sources.

In all cases PKSB 1934-638 (Reynolds, 1994) served as flux transfer calibrator and leakage reference. We performed standard delay, phase and bandpass calibration and transferred the solutions to PKS B0407-65 and 3C286, the latter from which crosshand solutions were derived. We additionally kept both the latter two calibrators phased up (diagonal phase solutions), because in L-band phase changes are the primary source of error. Flagging was performed with the RARG/SDP Tricolour (ADASS XXX accepted) flagger. We also very conservatively flagged scans by hand until we were satisfied with the spread of the amplitude, phase and real, imaginary components of the corrected visibilities. This was performed with the RARG FleetingPol pipeline (CASA 4.7 based). The table below summarizes the observations used for this study.

Epoch	obs. id(s)	min. elevation [deg]	max. elevation [deg]	Antenna hours	Wall time	flag %	Band
2017/04/13	1492094204	~20	~53	92:04:04	5:45:15	82.942	L
2017/04/21	1492794322	~21	~38	44:01:01	2:45:04	86.876	L
2017/05/01	1493665209	~20	~23	2:37:48	0:09:52	86.105	L
2017/06/23	1498145355	~20	~43	17:30:45	1:56:45	97.928	L
2017/07/23	1500817620	~21	~21	0:52:47	0:04:48	93.678	L
2017/07/25	1501002360	~20	~45	17:42:13	1:46:13	89.612	L
2017/09/08	1504941644	~17	~42	47:52:23	2:59:31	63.477	L
2017/09/24	1506241357	~16	~29	17:16:22	1:04:46	73.441	L
2017/09/26	1506418083	~17	~22	5:22:00	0:20:07	50.527	L
2017/10/26	1509002001	~18	~23	4:36:09	0:19:43	67.549	L
2017/11/18	1511048006	~18	~54	99:56:24	6:14:46	67.062	L
2017/12/29	1514570504, 1514902845	~37	~54	52:57:19	3:18:35	81.761	L
2018/03/04	1520185226	~16	~52	41:15:45	5:09:28	94.05	L
2018/04/07	1523128805, 1523101227, 1523102687	~21	~55	226:41:03	4:55:40	77.798	L
2018/05/29	1527617191	~16	~17	5:16:40	0:11:44	93.318	L
2018/05/30	1527694287	~16	~32	44:02:05	1:34:22	87.961	L
2018/09/04	1536060219	~16	~22	11:50:06	0:14:48	97.669	L
2019/03/02	1551564570	~21	~27	54:07:34	0:55:03	80.023	L

Derivation of the sky model at L-band is not excessively complicated, due to the off-axis sources contributing at maximum ~5% of the total field flux. We followed standard self-calibration procedure: a model is constructed within an automask (S. Makhathini) that masks out residual calibration correlation with the PSF that primarily affects the calibrator on boresight. The phase is then adjusted through delay and phase solutions until a final bandpass correction can be applied on a deeply cleaned model to minimize systemically biasing the fluxscale. All imaging is performed in the apparent scale with WSClean (Offringa, 2014).

At UHF the situation is more complicated. As already alluded to the off-axis flux density contributions to the to average field flux is not hour angle dependent and by bootstrapping the initial flux scale from a point source Reynolds model the flux scale of all the sources, on and off axis, are already biased. We provide a smooth fit to the spectrum of PKS B1934-638 itself from long tracks at L and UHF bands and compare this to the Reynolds coefficients.

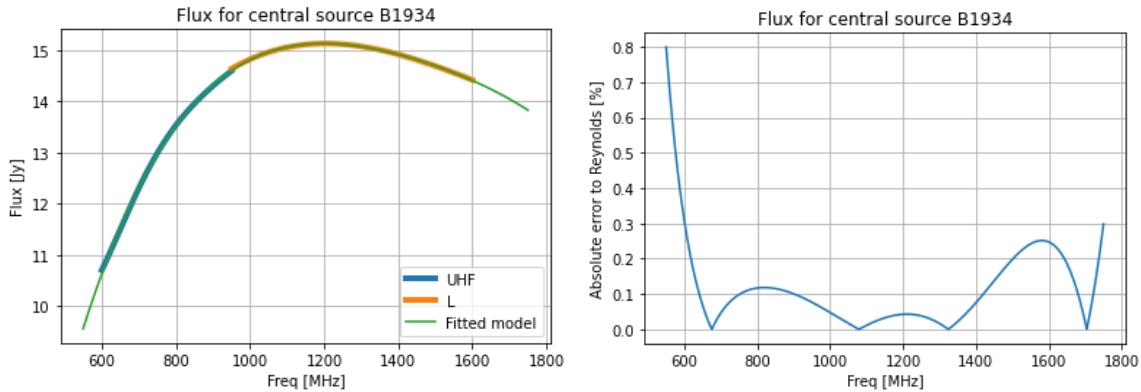


Figure 5: Model of central component of UHF all sky model (without contribution of off-axis sources) to compare the flux accuracy of the all-sky model to the original model used to calibrate the data. We note that the flux error is lower than 2% across most of the usable band.

As far as we know the absolute error of the Reynolds scale is not well quantified in the literature. This makes comparison to observations calibrated the scale of Perley and Butler (2017) hard because the absolute flux scale errors are unknown. We therefore used this opportunity to quantify the error in absolute flux scale by solution transfer onto J1331+3030 (3C286) and comparison to the flux scale quoted in Perley and Butler (2017). **The absolute error in flux scale is roughly 3% at the highest frequencies and up to 7% at the lowest frequencies of the U band. The difference between the Perley and Butler and Reynolds scale at 1.4GHz in L-band is about 2.2%, as taken from our long term co-observation of the sources.** This error is well within the 10% error permitted in the Perley and Butler scale and **therefore the Reynolds and PB scales may be used interchangeably between telescopes from the northern and southern hemispheres.**

4 Long term stability analysis

The long term stability of the primary calibrator is essential for accurate flux calibration. After excising the GPS and GSM subbands from the L-Band data we fitted a power law¹ to the flux densities of PKS B0407-65 (described in a separate followup memo) and 3C286 after derotating the calibrated data into feed relative frame:

$$S(\nu) = S_{1.4\text{GHz}} \left(\frac{\nu}{1.4\text{GHz}} \right)^{a+b \ln \frac{\nu}{1.4\text{GHz}} + c \ln^2 \frac{\nu}{1.4\text{GHz}}}$$

The deviation of the fitted 1.4GHz flux density from the median 1.4GHz is plotted in Figure 6. The comparison of transferred flux densities between 3C286 and PKS B0407-65 establishes that there are no significant flares on PKS B0407-65 of more than 5% during the campaign. The typical spread is no more than about 3%. The measured spread also establishes that all 3 calibrator sources are very stable.

¹ CASA setjy / Meqtrees spectral index convention

Modelling of PKS B 1934-638 (J193925.0-634245) as UHF and L-Band calibrator for MeerKAT	Doc No:	M2600-0000-043
	Rev No:	B

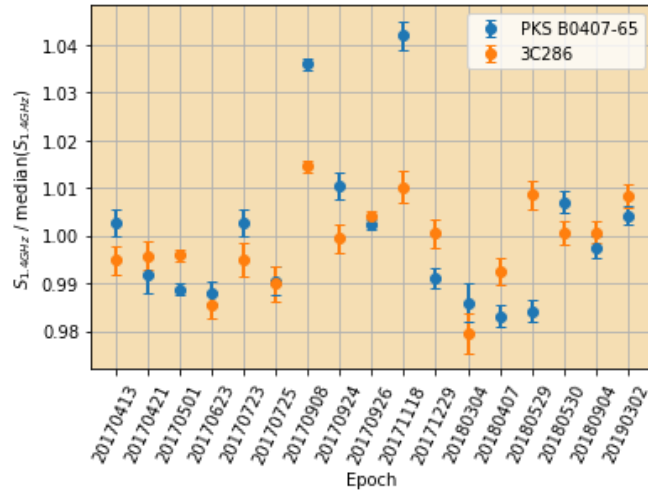


Figure 6: Long term stability of the sources bootstrapped from PKS B1934-638. This three-way comparison establishes that all sources are stable to well below 5% over the span of 2 years.

5 Field modelling of PKS B1934-638

5.1 UHF: Derivation of full sky model

In section 3 we outlined the calibration procedure used in data reduction. WSClean (A. Offringa) outputs a spectral model catalog when performing multi frequency synthesis imaging. The catalog has fitted components of the following convention²:

$$I(\nu) = I(\nu_0) + a(\nu/\nu_0 - 1) + b(\nu/\nu_0 - 1)^2 + \dots$$

The component list contains over 7000 delta scale components at robust factor -2 (near uniform weighted). The synthesized beam is 5.81"x5.38". The model has been derived to a detection limit of 7 sigma level (RMS noise 25μJy) at highest spatial resolution (uniform weighting).

This is a Multi Frequency Synthesis peak-to-noise ratio of about $\sim 5e^5$. We do note that the noise immediately next to the calibrator itself is much higher than the noise floor used for the signal to noise ratio. As we show later on in L-band these errors stem mostly from second order leakage effects.

A truncated version of the model is used for amplitude normalized phase calibration of the MeerKAT beamformer system. The limitations and system requirements are analysed in section 5.2. The MeerKAT image is shown in Figure 8.

² Standard can be found here: <https://sourceforge.net/p/wsclean/wiki/ComponentList/>

Modelling of PKS B 1934-638 (J193925.0-634245) as UHF and L-Band calibrator for MeerKAT	Doc No:	M2600-0000-043
	Rev No:	B

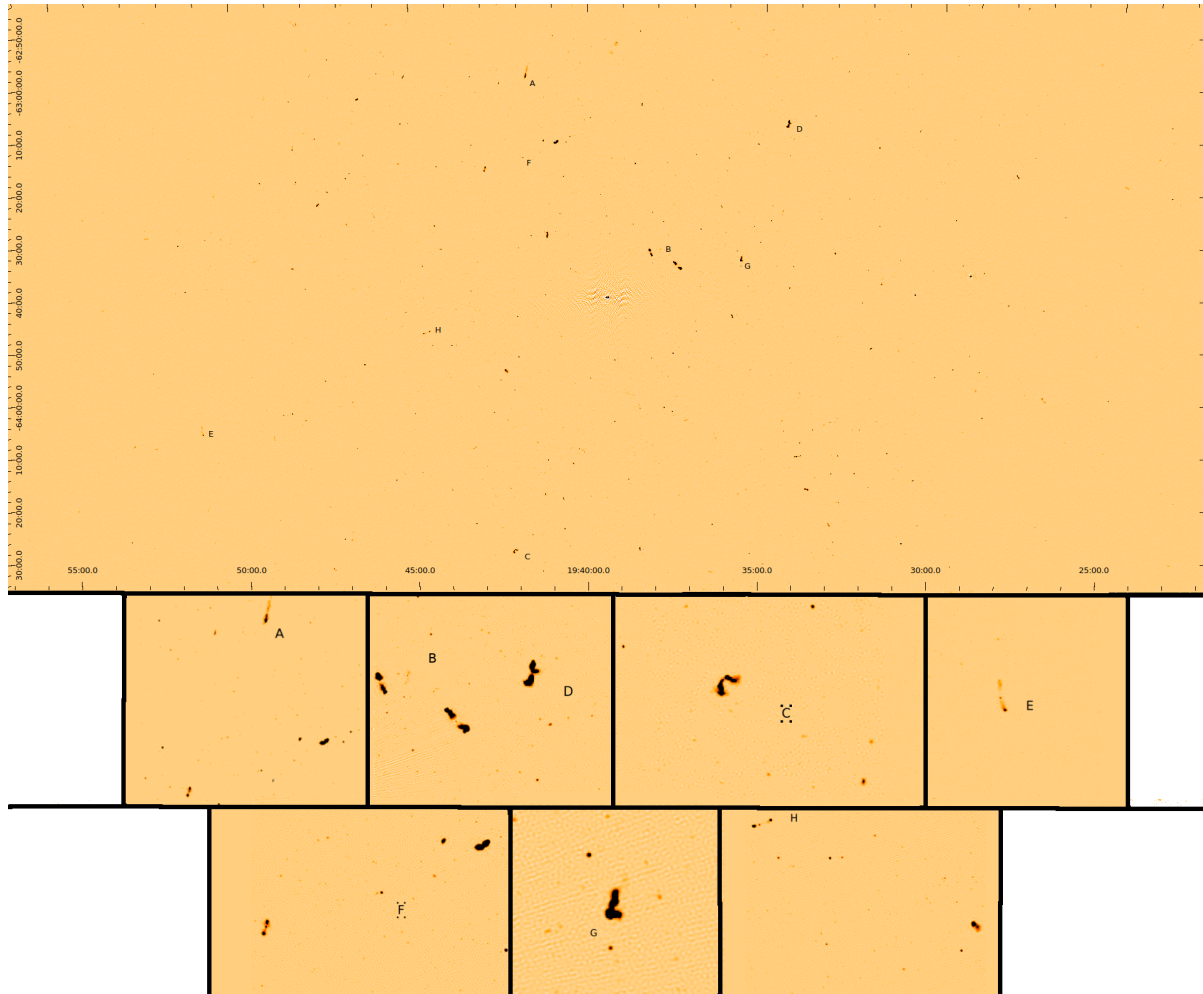


Figure 8: Field PKS B1934-638 and selected AGN morphologies in zoomed-in panels as observed with MeerKAT UHF band receivers. The full bandwidth is synthesized yielding a 25 μ Jy RMS noise level

5.2 UHF: System Equivalent Flux Density estimation

To aid planning of future observation we measure the array average UHF System Equivalent Flux Density (SEFD) from the primary calibrator field, PKS 1934-638, residual visibility noise over a span of elevations covering 49° to 41°.

Due to the large field of view it is important to account for the total foreground sky flux contribution in this field - **the result from using the full sky model is a reduction in the quotient phase by 43% compared to neglecting the contribution from the surrounding field sources.** We then use a uv continuum subtraction (CASA task uvcontsub with a 10th order fitting polynomial) to further fit the flux left over from the calibration errors on-axis from the primary source itself. Finally, the residual off-axis flux in the field is removed through (frequency discontinuous) FFT prediction in 12 degridting bands. The residual noise is shown in Figure 9.

Modelling of PKS B 1934-638 (J193925.0-634245) as UHF and L-Band calibrator for MeerKAT	Doc No:	M2600-0000-043
	Rev No:	B

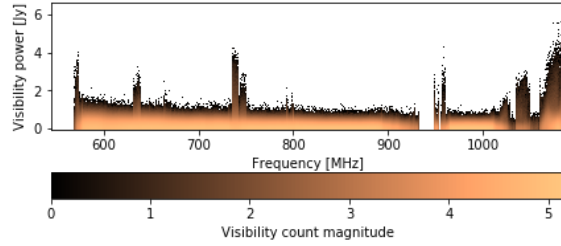


Figure 9: Residual visibility noise after subtraction of the surrounding field sources for the PKS B1934-638 field

We assume the standard unity convention for a perfectly calibrated linear feed MeerKAT system. The parallel hands measure (Smirnov, 2011)

$$\langle e_{p|}e_{q|}^* \rangle := I + Q$$

$$\langle e_{p-}e_{q-}^* \rangle := I - Q$$

The noise on a single hand σ_c (either $\sigma_{||}$ or σ_{--} , where $||$ and $--$ are shorthand for $\langle e_{p|}e_{q|}^* \rangle$ and $\langle e_{p-}e_{q-}^* \rangle$ respectively) measured by a baseline pq is given, for a particular integration τ_{int} and channelization $\Delta\nu$ for each of the cosine and sine correlators, as:

$$\sigma_c \propto \frac{\sqrt{\text{SEFD}_{pc}\text{SEFD}_{qc}}}{\sqrt{2\Delta\nu\tau_{\text{int}}}}$$

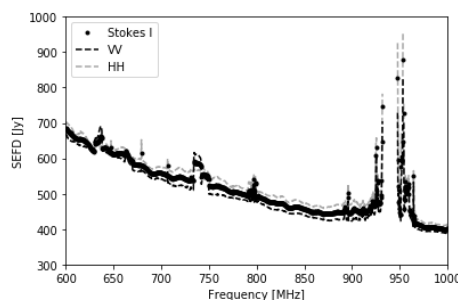
The noise of a Stokes I measurement by a uniformly illuminated dual hand system is then expressed as,

$$\sigma_I = \sqrt{0.5 (\sigma_{||}^2 + \sigma_{--}^2)}$$

This assumes covariances between $p|, p-, q|$ and $q-$ are all 0 if the signal is unpolarized and coupling can largely be ignored. We can then derive a first order estimate for the array average SEFD, by assuming roughly equal sensitivity between hands on all baselines pq and for all times, t (M such unflagged measurements in total)

$$\text{SEFD} \approx \sqrt{\frac{1}{M} \sum_{pq,t} \sigma_I^2 2\Delta\nu\tau_{\text{int}}}$$

The measured SEFD is shown in Figure 10.



Modelling of PKS B 1934-638 (J193925.0-634245) as UHF and L-Band calibrator for MeerKAT	Doc No:	M2600-0000-043
	Rev No:	B

Figure 10: System Equivalent Flux Density (SEFD) estimation for the UHF band based on the Reighley Jeans approximation. The derivation is based on residual visibility noise levels after subtraction of both the off and on-axis sources.

5.3 UHF: Application requirements for Science Processor UHF transfer calibration

From the SEFD estimation we can assuming that the VV and HH SEFD is approximately equal and with a fractional channel bandwidth of 132.8 kHz at UHF this places an effective bound on the calibration noise level of about 1.64mJy, 1.16mJy and 945µJy for calibrator scan lengths of 5, 10 and 15 minutes respectively. This assumes no tapering or removal of spacings during calibration. All sources at or above these levels must be accounted for during the bandpass calibration procedure in order not to bias the flux scale of the system - as mentioned before the first order terms are not hour angle dependent and are not washed out by fringe rotation.

The cumulative flux contribution, with priority to brighter emission is shown in Figure 11. The flux calibration error may be quantified based on the implementation efficiency limitations of the DFT based Science Processor pipeline, currently 90 components for online calibration. Here we show the fractional contribution to the total flux above the estimated noise at the bottom of the band where the combination of steep inverted GPS spectrum of the calibrator and the wide primary beam maximizes off axis contribution.

Although there are singular bright slightly resolved sources off axis, the majority of the off axis apparent flux is dominated by mJy level AGN population in the field, as shown in Figure 12 (to 95th percentile). This AGN population (much of which is well-resolved by the telescope) is responsible for the vast number of components needed to account for the cumulative flux shown above. Note that we refer to sources and components interchangeably for the intended purpose of this discussion.

In contrast to the constant average flux contribution of the off axis sources, the phase spread of the solution-absorbed ripples is strongly dependent on the cumulative super positions of the field source fringes. These fringes are hour angle dependent and are, therefore, subject to fringe washing. In worst case the fractional error in the argument from all sources above SEFD noise can be approximated as, where \oplus is the prefix scan (or accumulator) operator:

$$1 - \frac{4}{\pi} \tan^{-1} \left(\frac{\oplus(S_i w_i)}{\sum_i S_i w_i} \right)$$

The w_i terms here are the time-average amplitude response of the source, which scales as the square of the source separation distance from the interferometer phase centre. This means that the cumulative residual error is quickest minimized by including distance weighted flux contributions. This is shown in Figure 13 and is computed from the rectangular window approximation to smearing (shown in Figure 14 for the emission in this field) discussed in (Thompson, Moran & Swenson 2nd) - θ_b is the instrument resolution, r the separation cosine (approximated as radians in the small-angle approximation) and ω_e the sidereal rotation rate (rad/s):

$$w_i = 1.0645 \frac{\theta_b}{r \omega_e \Delta t} \operatorname{erf} \left(0.8326 \frac{r \omega_e \Delta t}{\theta_b} \right)$$

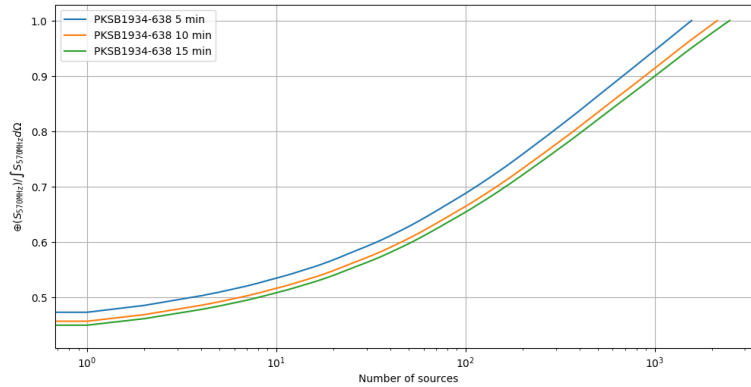


Figure 11: Cumulative fractional flux density contribution as a function of number of sources at 570 MHz.

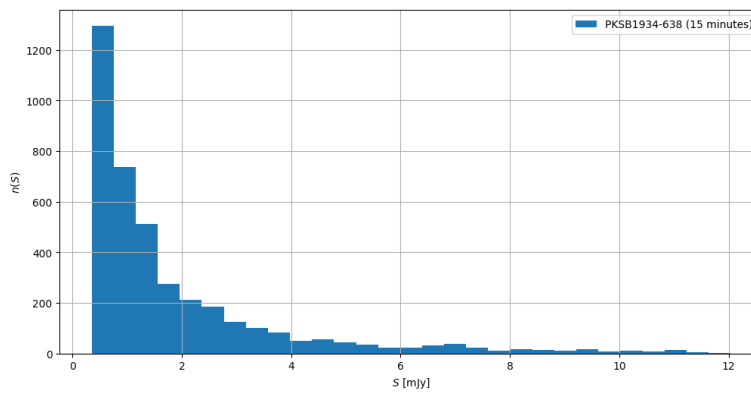


Figure 12: Distribution of flux densities of off axis sources up to 95th percentile. The majority of the sources are resolved. Furthermore, because of the high SNR of the image the high fraction of low flux density sources is also attributed to Star Formation Galaxies (SFG).

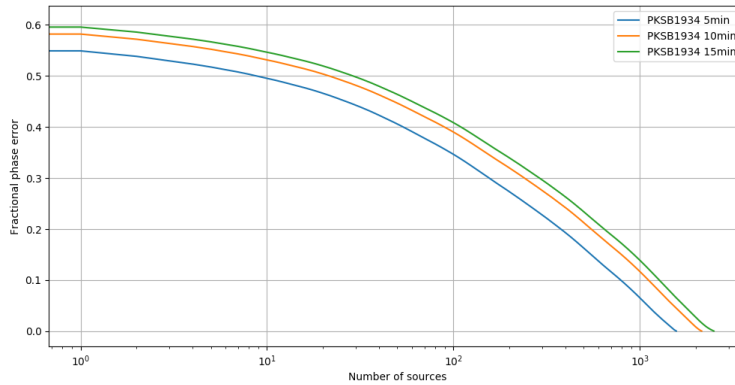


Figure 13: Fractional residual phase error as a function of number of sources.

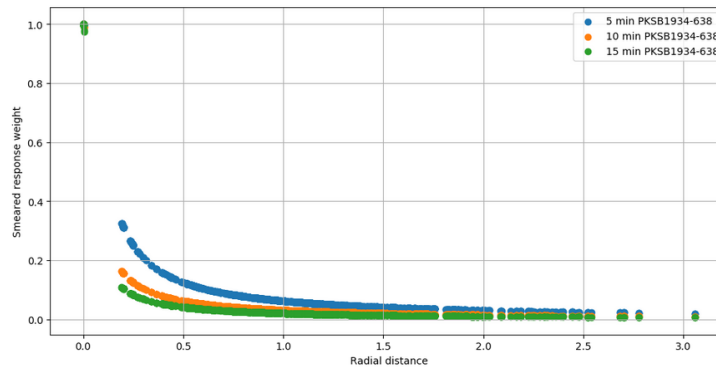


Figure 14: Estimated source smearing due to temporal fringe washing as a function of radius. 1.0 represents un-smearred sources.

5.4 Derivation of a companion L-Band full sky model and comparison to ASKAP

The L-Band image was synthesized using observations 1523128805, 1523101227, 1523102687 (2018/04/07). The extracted model was again constructed down to a local noise detection threshold of 7 sigma (RMS noise 22.5 μ Jy). The synthesized beam is 4.068" x 3.34" at robust -2 weighting. The peak to noise of this map 6.6e⁵. The apparent scale MeerKAT images are compared to the central region of an ASKAP apparent scale image below (priv. comm Emil Lenc, CSIRO).

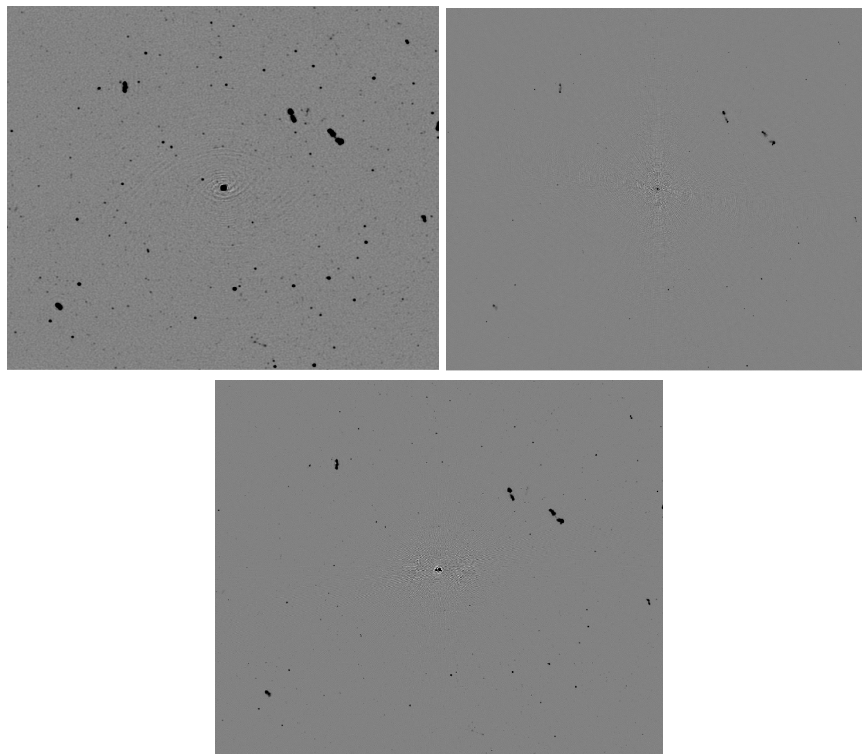


Figure 13: Three way comparison between ASKAP 887 MHz (top left), MeerKAT L-Band 1284 MHz (top right) and MeerKAT UHF Band 816 MHz (bottom). The slight extension seen in MeerKAT UHF band is likely a correlator smearing and/or imaging artifact. Overall the morphologies and astrometry is well matched.

Using pyBDSF (N. Mohan, 2015) ASKAP and MeerKAT sources positions are fitted and then crossmatched in a nearest neighbour algorithm. We find a systemic offset in the UHF positions of about 2" at the 25% percentile. Median plotted in dashed lines. This is indicated in Figure 14 and seems to indicate a systematic error. The final UHF catalog is corrected by the offset from the MeerKAT L-band catalog, as the MeerKAT L-band and ASKAP catalogs are closely matched in astrometry.

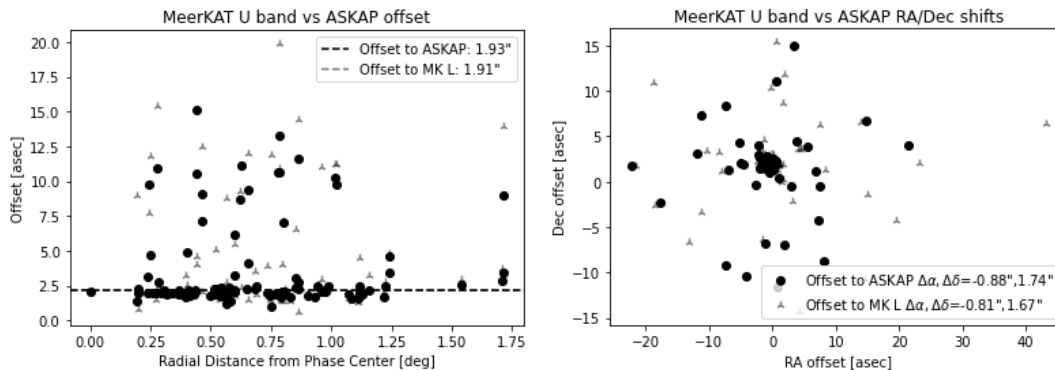


Figure 14: ASKAP and MeerKAT nearest neighbour positional crossmatch using positions fitted with pyBDSF. The negatives of the indicated offsets are added to the final catalog to correct for the apparent shift in astrometry in the UHF band

5.5 HDR imaging at L-Band

We find most of the calibration error at L-band stems from second order leakage effects - this is in contrast to our suspicions noted in the reduction process of [Modelling of primary calibrator J0825-5010 and incorporation into telescope phase-up](#). We have applied second order leakage corrections through CubiCal (Kenyon et al., 2018) 2x2 Jones solutions per channel and obtained dynamic ranges of 0.5m:1 in L-band immediately next to the calibrator itself. This shows that HDR calibration and imaging cannot viably be achieved using CASA at the time of writing, as the linearized equations implemented in it does not account for second order leakages (see Hales, 2017 for the linearized equations without second order effects). The differences in CASA self-calibration vs. self-calibration using CubiCal 2x2 solutions is shown in Figure 7 to the same scales. This has significant implications for e.g. cluster sciences where high dynamic range imaging is important to overcome sidelobe contamination from cluster AGN on surrounding diffuse emission.

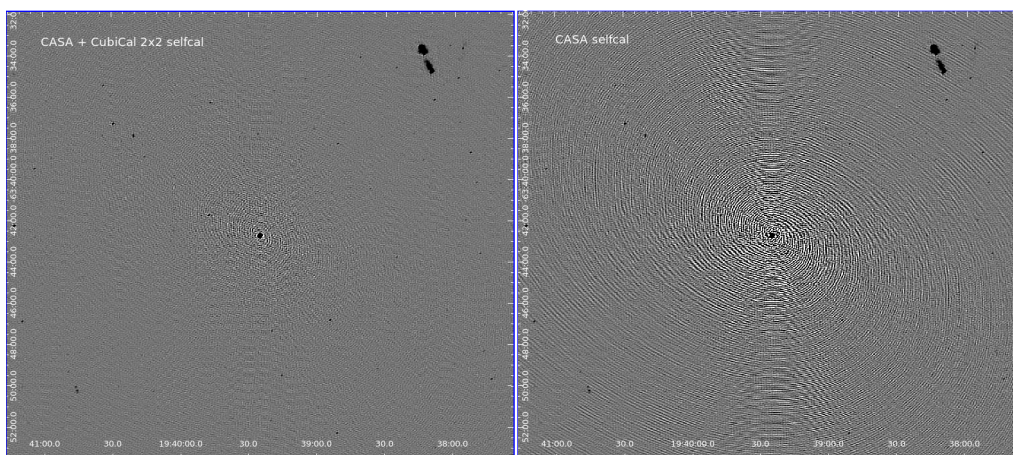


Figure 7: HDR image obtained by solving and applying 2x2 Jones solutions on this unpolarized field using CubiCal (left) after going as far as delay and amplitude self calibration using CASA (right). The improvement is substantial compared to using the linearized form of the RIME implemented in CASA and AIPS.

References

- Kenyon, J. S., et al. "CUBICAL—fast radio interferometric calibration suite exploiting complex optimization." *Monthly Notices of the Royal Astronomical Society* 478.2 (2018): 2399-2415.
- Offringa, A. R., et al. "WSCLEAN: an implementation of a fast, generic wide-field imager for radio astronomy." *Monthly Notices of the Royal Astronomical Society* 444.1 (2014): 606-619.
- Smirnov, Oleg M. "Revisiting the radio interferometer measurement equation-I. A full-sky Jones formalism." *Astronomy & Astrophysics* 527 (2011): A106.
- McMullin, Joseph P., et al. "CASA architecture and applications." *Astronomical data analysis software and systems XVI*. Vol. 376. 2007.
- Mohan, Niruj, and David Rafferty. "PyBDSF: Python Blob Detection and Source Finder." *Astrophysics Source Code Library* (2015): ascl-1502.
- Perley, Richard A., and Bryan J. Butler. "An accurate flux density scale from 50 MHz to 50 GHz." *The Astrophysical Journal Supplement Series* 230.1 (2017): 7.
- Reynolds J., "A Revised Flux Scale for the AT Compact Array", *ATNF Internal* (1994)
- Richard Thompson, A., James M. Moran, and George W. Swenson Jr. *Interferometry and synthesis in radio astronomy*. Springer Nature, 2017.
- Heywood, Ian, et al. "Field sources near the southern-sky calibrator PKS B1934-638: effect on spectral line observations with SKA-MID and its precursors." *Monthly Notices of the Royal Astronomical Society* 494.4 (2020): 5018-5028.

Appendix A

The catalogs discussed here can be found at:

<https://drive.google.com/file/d/1763ncsutS-UERNLCZ4bxb8rgYgypKkQb/view?usp=sharing>

The wsclean catalogs may be predicted using the Dask based Crystalball package (Serra and others, ADASS XXX accepted).

<https://github.com/paoloserra/crystalball>











Modelling of MeerKAT L and UHF band calibrators(2)


Final Audit Report

2021-03-11


Created:	2021-03-09
By:	Carmen Humphreys (carmen@ska.ac.za)
Status:	Signed
Transaction ID:	CBJCHBCAABAAID9Gn-BWBwbLyc3vv0T-b0cMKLIfZu4w

"Modelling of MeerKAT L and UHF band calibrators(2)" History

-  Document created by Carmen Humphreys (carmen@ska.ac.za)
2021-03-09 - 12:34:39 PM GMT - IP address: 105.224.208.78
-  Document emailed to Benjamin Vorster Hugo (bhugo@ska.ac.za) for signature
2021-03-09 - 12:35:52 PM GMT
-  Email viewed by Benjamin Vorster Hugo (bhugo@ska.ac.za)
2021-03-09 - 1:07:17 PM GMT - IP address: 66.249.93.202
-  Document e-signed by Benjamin Vorster Hugo (bhugo@ska.ac.za)
Signature Date: 2021-03-09 - 1:07:51 PM GMT - Time Source: server- IP address: 197.83.226.77
-  Document emailed to Thomas Mauch (tmauch@ska.ac.za) for signature
2021-03-09 - 1:07:54 PM GMT
-  Email viewed by Thomas Mauch (tmauch@ska.ac.za)
2021-03-09 - 1:08:58 PM GMT - IP address: 66.249.93.212
-  Email viewed by Thomas Mauch (tmauch@ska.ac.za)
2021-03-10 - 1:43:46 PM GMT - IP address: 66.249.93.210
-  Document e-signed by Thomas Mauch (tmauch@ska.ac.za)
Signature Date: 2021-03-11 - 7:57:38 AM GMT - Time Source: server- IP address: 196.24.39.242
-  Document emailed to Sharmila Goedhart (sharmila@ska.ac.za) for signature
2021-03-11 - 7:57:41 AM GMT
-  Email viewed by Sharmila Goedhart (sharmila@ska.ac.za)
2021-03-11 - 8:18:24 AM GMT - IP address: 66.249.93.213

 Document e-signed by Sharmila Goedhart (sharmila@ska.ac.za)

Signature Date: 2021-03-11 - 8:18:54 AM GMT - Time Source: server- IP address: 169.0.109.174

 Agreement completed.

2021-03-11 - 8:18:54 AM GMT